ISTITUTO NAZIONALE DI RICERCA METROLOGICA
Repository Istituzionale

Bioresorbable fibers for interstitial null-separation diffuse optical spectroscopy using fast temporal gating

(Article begins on next page)

23 February 2025

Journal of Physics: Photonics

CrossMark

PAPER

Bioresorbable fibers for interstitial null-separation diffuse optical spectroscopy using fast temporal gating

Vamshi Damagatla[1], Nadia G Boetti[2], Laura Di Sieno[1,*], Diego Pugliese[3,4], Ilaria Bargigia[1,5], Davide Janner[4], Alberto Dalla Mora[1] and Antonio Pifferi[1,6]

1 Politecnico di Milano, Dipartimento di Fisica, Milano, Italy
2 Fondazione LINKS—Leading Innovation and Knowledge for Society, Torino, Italy
3 Istituto Nazionale di Ricerca Metrologica (INRiM), Torino, Italy
4 Politecnico di Torino, Dipartimento di Scienza Applicata e Tecnologia and INSTM research unit, Torino, Italy
5 Center for Nano Science and Technology@PoliMi, Istituto Italiano di Tecnologia, Milano, Italy
6 Istituto di Fotonica e Nanotecnologie, Consiglio Nazionale delle Ricerche, Milano, Italy
* Author to whom any correspondence should be addressed.

E-mail: laura.disieno@polimi.it

Abstract

Bioresorbable fibers are an exciting prospect as probes and implants to provide optical access to the human body. In this work, we demonstrate interstitial spectroscopy with bioresorbable fibers at null distance, using time-domain diffuse optics that disentangles absorption from scattering properties and probes the tissues up to a depth of a few cm around the fiber tips. We exploit a fast-gated single-photon avalanche diode with >55 dB of dynamic range to overcome the burst of 'early' photons hiding the information of absorption from deep tissues. We tested the absorption linearity—retrieving the water spectrum in the 700–950 nm range with >85% accuracy over two decades of absorption change—and verified the hypothesis of a scattering-independent absorption retrieval. Further, we were able to detect spectral changes at a distance of 1 cm from an inclusion embedded in a biological tissue. Time-domain diffuse optical spectroscopy with bioresorbable fibers could detect spectral changes without being affected by blood extravasation at the fiber tips and could help for long-term monitoring in tissue healing, thermal treatment, photodynamic therapy and ultimately, towards minimally invasive medical procedures.

1. Introduction

Since 600 BCE, when Sushrutha, the founding father of surgery pioneered medical surgeries and implants, to the 19th century when science fiction first made its foray courtesy Mary Shelly's 'Frankenstein', people have always been fascinated by the concept of artificially modifying the human appearance and structure, through implantable organs, supports, mechanics, sensors, devices and chips. However, some of the biggest challenges to such devices were not their functional physics or the minuscule electronics, but more importantly, their biological compatibility, i.e. a need to be non-toxic to the surrounding tissue in short and long term.

With the successful introduction of implantable medical devices in the late 1950s [1], the next revolution in the field of medical implantation has perhaps been the advent of bioresorbable materials that aim not just to be biocompatible but also biologically resorbable in tissue. Bioresorbable materials have been gaining widespread interest and importance over the past few decades in the medical field for their use as implants, support casings and in general for their compatibility and resorbability in biological tissue. It is the key feature which allows a material to disintegrate into harmless components in the human body. A well-known example that has been exploited is the use of self dissolving medical stitches [2]. This feature has also been extremely desirable in production of orthopedic implants aiming to reduce intrinsic problems of metallic implants such as stress-shielding, pain, irritation, endogenous infection of surrounding bone tissue, etc [3, 4]. These mechanical implants such as screws, plates, etc have been considered useful to avoid surgical intervention for implant removal. However, the need for not just mechanical support but also sensing

capabilities has lead to the research and development of many kinds of materials for this purpose including silks, single and polycrystals, glasses, glass–ceramics, polymers and composites [5, 6].
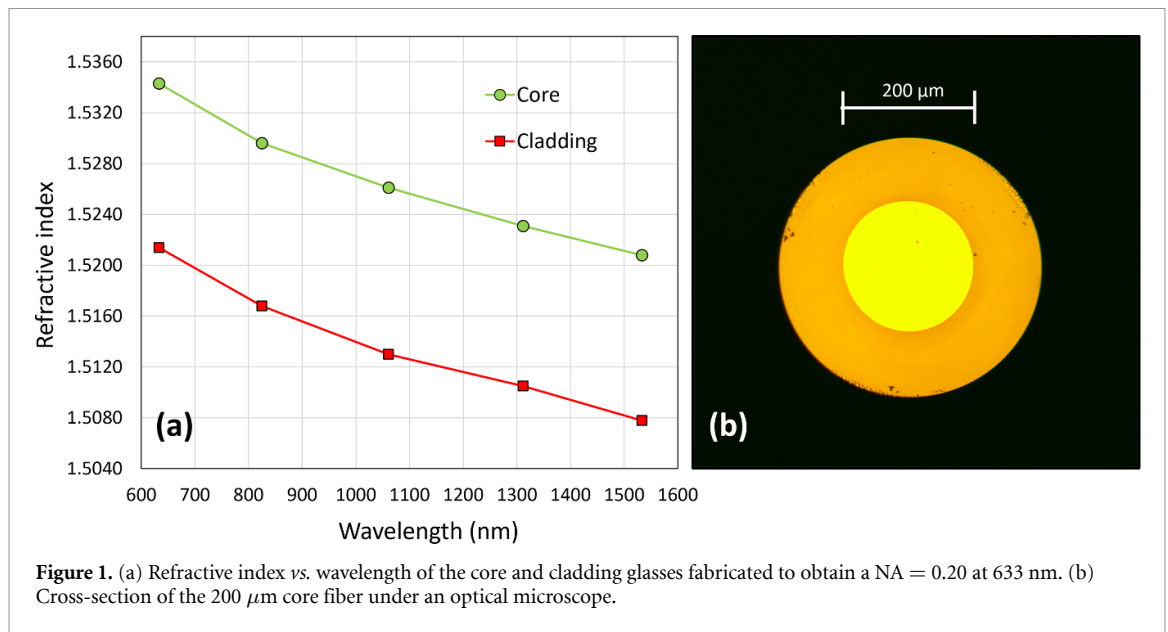
The availability of bioresorbable glasses enabled photonics to enter the field with the preparation of bioresorbable optics and fibers. Over the years, many types of optical components have been developed, such as microlens arrays, photonic crystals, diffraction gratings and optical fibers [7–10]. In particular, biocompatible and resorbable fibers made of calcium phosphate glass (CPG) pave the way for fiber optic implantation and unveil perspectives in the field of biophotonics for many applications such as—endoscopic monitoring [11], optical biopsy and organ monitoring [12], photodynamic therapy monitoring [13, 14], thermal treatment monitoring [15], drug diffusion, post surgical internal observation, among others [16]. These glasses also have the dual advantage of being self-dissolving in case of internal breakage during their implantation period inside the body. However, the mentioned applications also imply a need to perform measurements in an interstitial scenario, i.e. where the fibers are inserted into the body at single [17, 18] or multiple positions [19], and this is often referred to as interstitial fiber spectroscopy (IFS)/imaging depending on the application. IFS has the potential to be used for medical applications as a guidance tool in minimally invasive surgical procedures.

A plethora of techniques have attempted to provide information in an interstitial setting, but in most cases are point-based and are able to obtain information from a region either in front of or very close to the fiber or probe tip. In this context, the field of diffuse optics (DO) provides a means to probe deeper into the tissue by allowing us to retrieve information from diffusely distributed photons. Diffusive optics has been explored since many years as a technique to probe the human tissue through different directions such as the continuous wave [20], frequency-domain [21] and time-domain (TD) [22] approaches. In particular, TD diffuse optical spectroscopy (TD-DOS) – based on the detection of the distribution of time-of-flight (DTOF) of photons traveling into the tissue—presents several additional advantages: (i) the ability to disentangle the absorption coefficient μ_a and the reduced scattering coefficient μ_s'; (ii) comparatively larger probed depths (in the order of a few cm); (iii) insensitivity to amplitude fluctuations, which could be useful to remove effects of laser fluctuations or bleeding near the fiber tip [22–26].

In the case of IFS, both the source and detection channels should preferably be hosted in a single needle to reduce the invasiveness, and this scenario is known as the null source-detector separation (NSDS) approach in TD-DOS [27]. This is indeed unusual in standard TD-DOS measurements, where the source and the detection fibers are separated by a few cm so as to collect the diffuse photons which have explored deeper tissue regions. But, in principle, in TD-DOS the explored depth is solely dependent on the photon's traveling time, thus making spatial sampling feasible even at NSDS [28, 29]. In addition, NSDS offers better contrast, spatial resolution, and increased signal [27, 30, 31]. However, the burst of 'early' photons can saturate classical detection approaches, hindering information about the absorption and depth [32]. Thus, TD NSDS measurements call for a detection mechanism with a high dynamic range, and we achieve it using the principle of 'hardware gating' by utilizing a fast, temporally gated detector with an ability to be turned off and on extremely quickly, hence being able to reject the early photons. Fast-gated single-photon avalanche diodes (FG-SPADs) have been developed at Politecnico di Milano, and have been demonstrated for high-dynamic range measurements at small source-detector separations for functional brain activation imaging, and for non-contact DO imaging [31, 33–35]. In this work, we aim to combine all these different aspects—bioresorbable fibers, interstitial NSDS measurements and broadband spectroscopy—to perform broadband, interstitial, null-separation spectroscopy on biological phantoms. The suitability of CPG fibers for TD-DOS has already been demonstrated through the MEDPHOT [36] and BIP [37] protocols, and spectroscopy in standard configurations [38, 39]. In this paper, we will exploit further the use of these CPG fibers for TD-DOS, and demonstrate for the first time IFS with the CPG fibers, with the source and detection fibers at an inter-fiber distance of $\rho = 0$. In the following, we will first briefly describe the preparation of the fibers, followed by a description of the experimental setup used and the analysis methods employed—in particular, a description of the 'scattering-independent absorption retrieval' method. Then, we present the basic testing of the system as per the MEDPHOT protocol [36] and also prove the scattering independence of the absorption spectra on liquid phantoms. Finally, we test this approach in a more realistic biological scenario by attempting to detect spectrally the presence of an absorbing inclusion in a heterogeneous medium.

2. Fabrication of the bioresorbable fiber

The bioresorbable optical fiber employed for this research was fabricated by preform drawing, with the preform being obtained by the rod-in-tube technique. The core and cladding glasses were synthesized starting from high purity ($>99\%$) chemicals (P_2O_5, CaO, MgO, Na_2O, B_2O_3, SiO_2), which were weighed and mixed inside a glove box under dried air atmosphere to minimize the hydroxyl ion (OH^-) content in the

Figure 1. (a) Refractive index *vs.* wavelength of the core and cladding glasses fabricated to obtain a NA = 0.20 at 633 nm. (b) Cross-section of the 200 μm core fiber under an optical microscope.
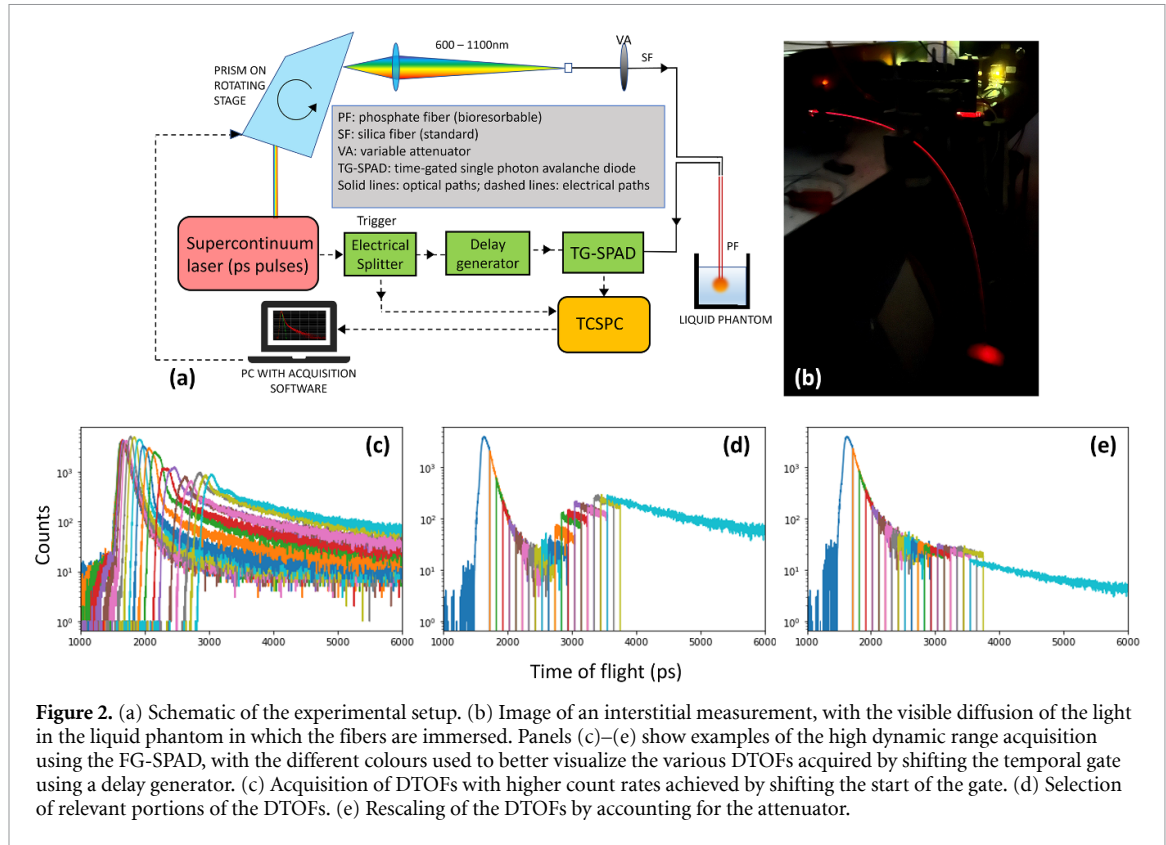
glass. They were then transferred into an alumina crucible for melting in a vertical furnace at a temperature of 1200 °C for 1 h under a controlled atmosphere (dry air, water content <3 ppm). The refractive indices of the core and cladding glasses were measured at five different wavelengths (633, 825, 1061, 1312, 1533 nm) with a Metricon 2010 prism coupler and are shown in figure 1(a). At 633 nm the refractive indices of the core and the cladding revealed to be 1.5343 ± 0.0005 and 1.5214 ± 0.0005, respectively, corresponding to a fiber numerical aperture (NA) value of 0.20. The core glass was then cast into a cylindrical mold to form a 12 mm diameter rod, while the cladding tube was shaped by extrusion using an in-house developed equipment. The core-cladding preform was obtained by inserting the stretched core into the cladding tube, and then the optical fiber with dimensions of 200/400 μm for the core and cladding, respectively, was drawn from the assembled preform. The drawing tower furnace (SAET, Turin, Italy) consists of a graphite ring heated by induction operating at 248 kHz and delivering 170 W to reach the required drawing temperature. The quality and morphology of the fabricated phosphate glass optical fiber were inspected by means of a Nikon ECLIPSE E 50i optical microscope and the cross-section of the phosphate glass fiber is shown in figure 1(b). The core/cladding interface was found to be of high quality and no sign of crystallization was observed. Detailed information on the bioresorbable glass and thermo-mechanical and optical properties of the fiber, as well as dissolution studies performed in phosphate buffer solution, are described in other works [9, 40].

3. Methods

3.1. Experimental setup

The experimental setup used (figure 2(a)) was similar to a state-of-the-art TD-DOS system [41, 42] developed at Politecnico di Milano and can be divided into two parts—the source arm and the detection arm. On the source arm, a supercontinuum source with a picosecond laser pulse generator at 40 MHz pulse frequency (SuperK Extreme, NKT Photonics) was used to generate pulses, which were spatially dispersed by a Pellin Broca prism mounted on a calibrated rotating stage to separate the components of the supercontinuum spectrum (550–1900 nm). They were consequently focused and coupled into a 50/125 μm graded-index fiber. The wavelength range used was from 600–1000 nm and was scanned in steps of 20 nm, with a linewidth varying from 3 nm at 650 nm up to 8 nm at 1000 nm. Light injection and collection into and from the medium, respectively, were achieved through a pair of 200 μm core phosphate glass fibers, placed on the surface of the sample. A variable attenuator was inserted via an U-bracket on the injection path to modulate the input power and keep the resulting count rate within single-photon statistics. The collecting fiber was then coupled through a 200 μm silicon fiber onto the active area of the detector, and the DTOFs were processed using a time-correlated single photon counting (TCSPC) module (SPC-130, Becker and Hickl). The detection mechanism is based on a 100 μm Si SPAD enabled in fast-gating mode [43]. The detector can be turned on in few hundreds of ps and kept on for a given period. This possibility allows one to record only a portion of the DTOF. This window of measurement is the hardware-enforced temporal gate, and is the starting point for high dynamic range acquisition. Indeed, while keeping the count-rate constant for each gate, it is possible to increase the power injected in the medium when acquiring the later parts of the

Figure 2. (a) Schematic of the experimental setup. (b) Image of an interstitial measurement, with the visible diffusion of the light in the liquid phantom in which the fibers are immersed. Panels (c)–(e) show examples of the high dynamic range acquisition using the FG-SPAD, with the different colours used to better visualize the various DTOFs acquired by shifting the temporal gate using a delay generator. (c) Acquisition of DTOFs with higher count rates achieved by shifting the start of the gate. (d) Selection of relevant portions of the DTOFs. (e) Rescaling of the DTOFs by accounting for the attenuator.

DTOF (i.e. late photons). Each slice of the acquired DTOF is divided by the annotated laser attenuation to reconstruct the DTOF with a much larger dynamic range, thus avoiding the constraints of the single-photon statistics and saturation of the detector. To reconstruct the DTOF (figures 2(c)–(e)) we applied 20 subsequent gates at steps of 100 ps delay with a total shift of the opening window of 2000 ps. On the other hand, the instrument response function (IRF) was acquired with 40 gates of delay, at steps of 50 ps each to have a better sampling of the fast tail. In using this acquisition strategy, we were able to acquire >55 dB of dynamic range. Detailed information on the working mechanism and characterization of the detection system can be found in other works [43].

3.2. Analysis

The analysis of the DTOFs was performed using a solution of the radiative transport equation under the diffusion approximation [44, 45]. For an infinite homogeneous medium the analytical TD Green's function solution for the fluence is given by equation (1), where, $D = \mu'_s/3$ is the diffusion coefficient and v is the speed of light in the medium

$$\phi(\vec{r}, t) = \frac{v}{(4\pi Dvt)^{3/2}} \exp\left(-\frac{\rho^2}{4Dvt}\right) \exp\left(-\mu_a vt\right). \tag{1}$$

For the case of the NSDS approach, where the source-detector distance is $\rho = 0$, it has been shown that, under the diffusion approximation, the effect of the scattering vanishes, leaving the fluence independent of μ_a as shown in equation (2), where $K = v/(4\pi Dv)^{3/2}$ is a constant that does not affect the analysis due to the need for normalization of DTOFs [46]

$$\phi(\vec{r}, t) = Kt^{-3/2} \exp\left(-\mu_a vt\right). \tag{2}$$

We had verified this approximation previously by comparing it to the gold standard—Monte Carlo simulations—showing that at later times the Monte Carlo simulations and the simplified fluence (equation (2)) for the homogeneous medium have negligible differences. Consequently, we had hypothesized and verified experimentally, the scattering-independent absorption retrieval by taking into account for analysis only the late photons with longer time-of-flight [46]. This approach is followed also in the present paper. The absorption properties of the medium were retrieved using an inversion procedure by convolving the analytical solution of the diffusion equation (DE) with the IRF and fitting it to the experimental DTOFs through a non-linear optimization using the Levenberg–Marquardt algorithm [47]. Generally, the best fits

are obtained by varying and optimizing the freely varying parameters (μ_a, μ_s') and the fitting range. In this case however, as discussed above, μ_s' was kept constant and both μ_a and the fitting range were varied to recover only the absorption values. The fitting range is defined as a fraction of the peak count on the rising ('−' sign) and falling edge ('+' sign). In particular, we varied the beginning of the fitting range from + 0.1 down to + 0.0001 (thus overcoming the peak containing the early photons and beginning the fitting on the tail of the DTOF), whilst fixing the falling edge to + 0.000008.

3.3. Samples

Two types of samples were prepared for the experimental campaign: liquid phantoms and biological samples. The liquid phantoms used were aqueous dilutions of intralipid (IL) and ink, prepared to get the desired optical properties [48]. The biological phantoms were constructed using meat and fat tissues, which were first measured with an existing state-of-the-art TD-DOS system to determine their optical properties [41]. Three types of measurements were performed - (i) to test the absorption linearity of the system; (ii) to test scattering-independent absorption retrieval of the water spectrum; (iii) to spectrally detect the presence of an inclusion in a background medium. For the linearity measurements, a liquid phantom was prepared with a fixed scattering value of $\mu_s' = 10 \text{ cm}^{-1}$ at 700 nm while the μ_a was altered by adding calculated values of ink. To test the scattering independence for experiment (ii), three IL phantoms were prepared with $\mu_s' = 10, 15$ and 20 cm^{-1} and no added absorption apart from the water absorption. For the biological phantoms (iii), the inclusions used were cubes of speck (processed porcine leg meat) of dimensions $2 \times 2 \times 2 \text{ cm}^3$, cut so as to contain as less of the visible white fat as possible. These inclusions were then placed into two different backgrounds. In the first case, the background was a dispersion of IL in water with $\mu_s' = 10 \text{ cm}^{-1}$ at 700 nm contained in a tank of $24 \times 16 \times 12 \text{ cm}^3$. The inclusion was placed in the tank with a minimal base support such that the top surface of the inclusion was at a depth of 5 cm in the liquid phantom. In the second case, the background was a block of solid, porcine processed fat of dimensions $14 \times 10 \times 7 \text{ cm}^3$ (hereon referred to as lard), and the inclusion was placed at a depth of 4.2 cm from the surface of the background.

4. Measurements on liquid phantoms

The system was first assessed by performing linearity measurements as defined in the MEDPHOT protocol [36]. A series of measurements were performed on the IL phantoms described in the samples section by changing the absorption of the medium. We had 8 additions of ink corresponding to greater than a 100 fold increase in concentration. Further, choosing two different wavelengths of 705 and 805 nm and taking into account the inherent water absorption of the phantom, it gave us an expected rise in absorption of about 2 orders of magnitude. Figure 3(a) shows the absorption linearity of the system at two wavelengths. Barring a few outliers for low absorption phantoms at 805 nm, the system was found to be linear in recovering the μ_a, within a relative error of 20% for a change in μ_a across about 2 orders of magnitude. We tested the scattering-independent absorption retrieval by attempting to retrieve the absorption spectrum of water from the IL phantoms, independent of their μ_s'. As can be seen from figure 3(b), in the wavelength range of 700–940 nm, the water spectrum was assessed with less than 14% relative error as compared to literature. Furthermore, the retrieved absorption was obtained fitting the measurements without including any scattering even if three different values of $\mu_s' = 10, 15$ and 20 cm^{-1} were used. We aimed to measure the spectra across the spectrum from 600 up to 1000 nm, however, there exist some discrepancies in certain ranges. Below 700 nm, the high relative error could be due to the following reasons: (i) low absolute values of absorption ($\approx 10^{-3} \text{ cm}^{-1}$); (ii) effect of boundaries in the assumed infinite medium; (iii) residual absorption by lipid molecules (around 4.3% in weight). On the other hand, above 940 nm, we were hampered by the efficiency drop of silicon SPADs. Combining this with the high absorption of the water peak at 980 nm and limited laser power leads to the slope of the measurement DTOF becoming similar to the slope of the IRF, thus not allowing us to retrieve any information.

5. Measurements on biological inclusions

The aim of the biological inclusion phantom measurements was to see if we could detect the presence of an inclusion as a function of the depth of the probe. In an interstitial setting, this could be a useful depth guidance tool for minimally invasive surgery to detect abnormalities, tumors, organs, etc. As described in the samples section, the inclusions were placed at a depth of 5 and 4.2 cm from the surface of the water + IL or lard matrix, respectively. The fibers were inserted into the background medium at a starting position of 2 cm above the surface of the inclusion (3 cm from the surface of the liquid sample) and spectral measurements were taken.
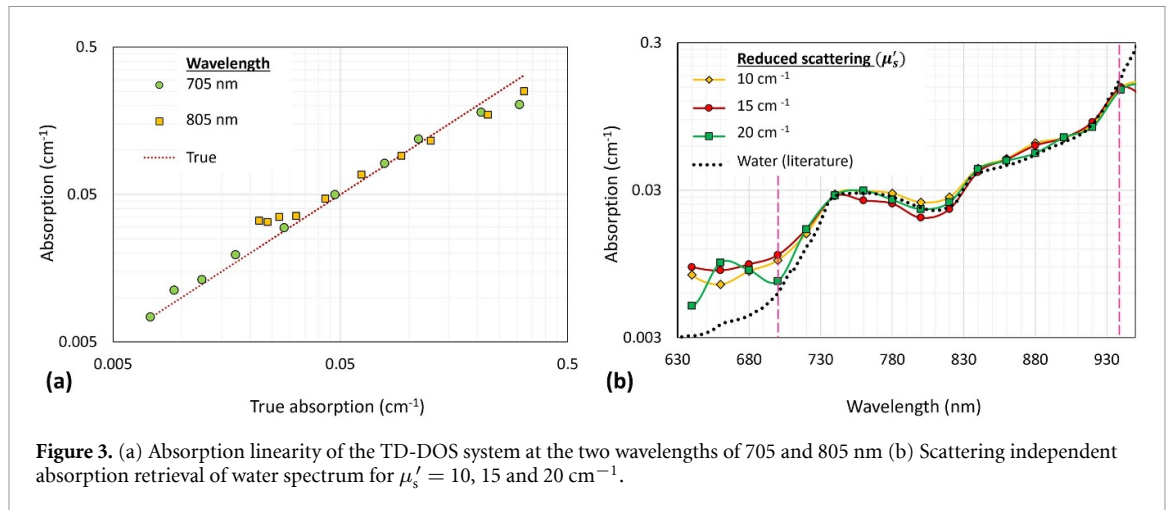
Figure 3. (a) Absorption linearity of the TD-DOS system at the two wavelengths of 705 and 805 nm (b) Scattering independent absorption retrieval of water spectrum for $\mu_s' = 10$, 15 and 20 cm^{-1}.
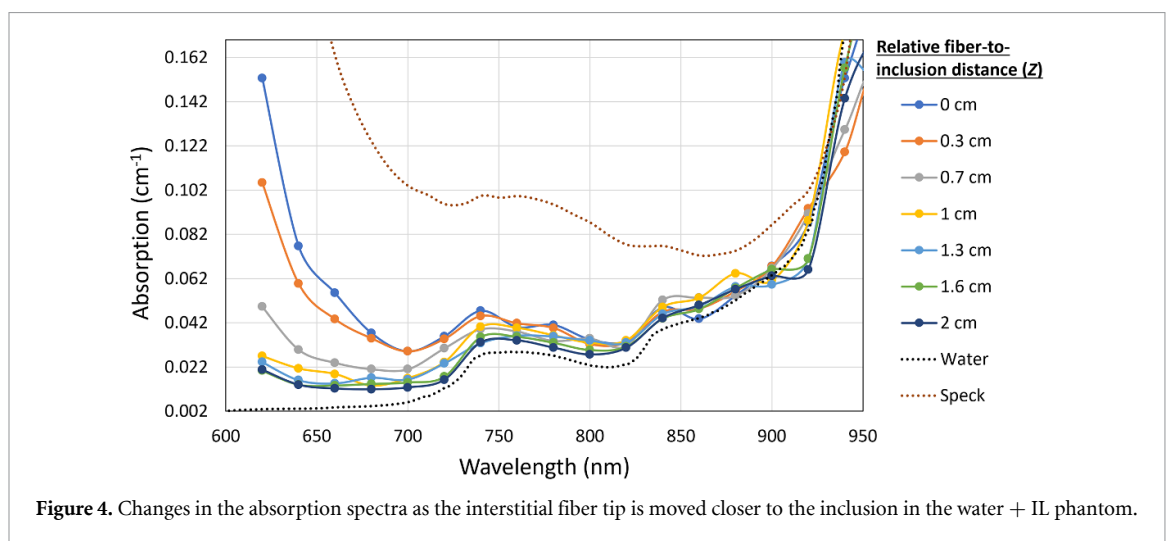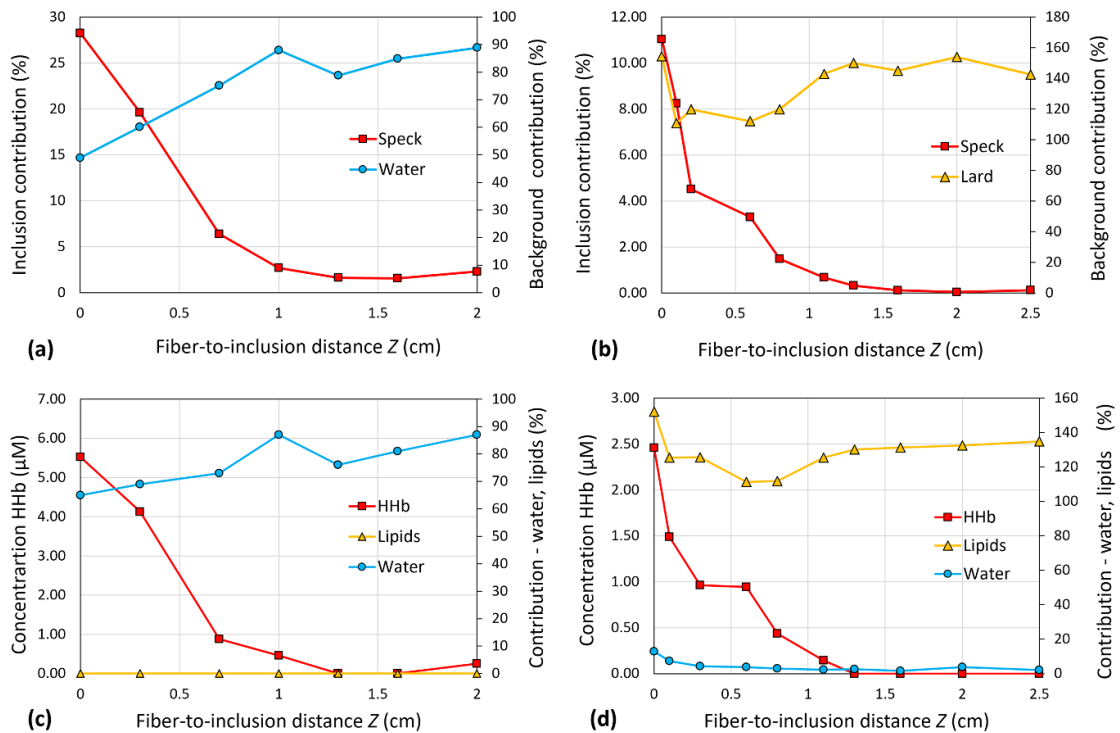

Figure 4. Changes in the absorption spectra as the interstitial fiber tip is moved closer to the inclusion in the water + IL phantom.

Subsequent spectra were acquired, moving the fibers towards the inclusion at steps of 0.3/0.4 cm till the fiber tips reached the upper surface of the speck specimen, thus reducing the relative distance of fiber-to-inclusion (Z) from 20 mm down to 0 mm. This process was repeated for both backgrounds. The retrieved spectra for the speck embedded in a water + IL background are shown in figure 4 for different values of Z (solid lines). The reference spectra of the background and the inclusion are also shown as dotted lines. As the distance Z decreases, there is an increase in the absorption, mostly in the region <850 nm, which can be ascribed to the blood-related components of speck [49]. Conversely, for wavelengths below 900 nm, the key absorber of both the inclusion and the background is water. Above 940 nm the retrieved spectra becomes unreliable as discussed before. Some first hints on the presence of the inclusion are observed at $Z = 1$ cm, while a clear detachment is seen at around $Z = 0.7$ cm. When the fibers touch the inclusion, its spectral features are markedly observed, though the contamination of the background medium is clearly seen. Figure 5 displays the spectra for the speck inclusion embedded in a lard matrix. Also here, solid lines represent the spectra retrieved at different distances Z from the inclusion, while dotted lines indicate the reference spectra of the background (lard) and the inclusion (speck). It must be noted that here we are able to measure up to 1000 nm, as the background matrix of lard has much lower absorption unlike that of pure water as in the previous case. Upon reducing the fiber-to-inclusion distance Z, the spectral fingerprints of the speck specimen, that are the blood-related absorption in the wavelength region <700 nm and water contribution around 980 nm, appear clearly as in contrast to the background of the lipid spectrum. Also in this case, when the fibers are in contact with the inclusion, the spectrum is still strongly affected by the surrounding background medium, as expected since the fibers are just on the surface of the inclusion.

As a further qualitative validation, we attempted to fit the obtained spectra with the individual absorption spectra of the inclusion and the background, to obtain a relative estimate of their contribution to the overall spectrum. Figures 6(a) and (b) show the percentage contributions for the speck inclusion in the water + IL and lard background matrices, respectively. The trends evidently indicate the presence of the
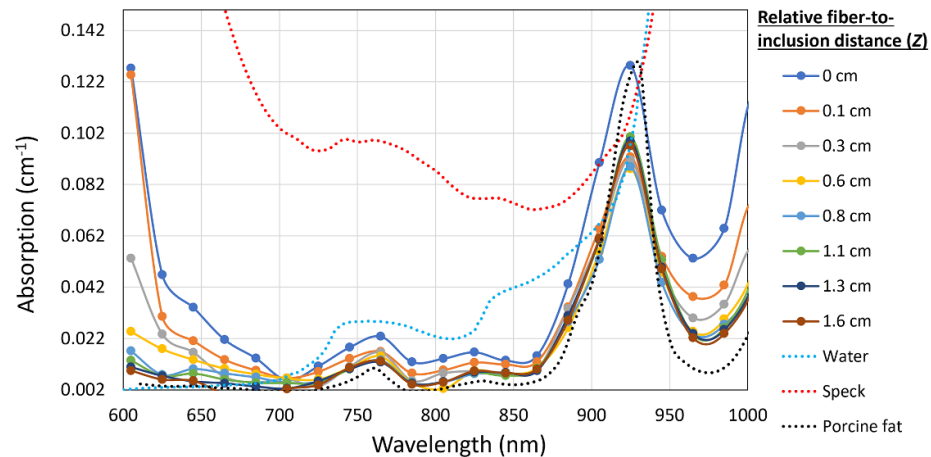
Figure 5. Changes in the absorption spectra as the interstitial fiber tip is moved closer to the inclusion in the porcine fat phantom.

Figure 6. Change in contribution to the absorption spectra with the movement of the interstitial probe towards the speck inclusion in (a), (c) water + IL background and (b), (d) lard matrix. While panels (a) and (b) show the contributions in terms of the spectra of background and inclusion samples, (c) and (d) show the contribution in terms of commonly observed chromophores—haemoglobin, water and lipids.

inclusion to be visible from a fiber-to-inclusion distance of 10 mm. The contribution due to the inclusion keeps increasing as Z goes to 0, whereas the relative contribution due to the background starts to decrease from $Z < 10$ mm. While the sum of contributions for the speck in water + IL background is less than 100%, it is however greater than 100 for the lard matrix. These values are indeed non-physical and can attributed to various factors such as: (i) noisy spectra due to more coarse sampling of the data (20 nm) as compared to the reference spectra (5 nm); (ii) use of a homogeneous rather than a perturbative model for fitting of optical properties; (iii) the spectra of the inclusion and the background are not orthogonal as the inclusion contains some lipids and water; (iv) spectral data in the range 940–1000 nm are used to track the contributions due to the water peak at 980 nm, however, due to the small size of the inclusion, we notice only an increase in absorption and not the actual peak feature. This causes the spectral fitting (depending dominantly on shape and peak features) to overestimate the lipid content to compensate for this contribution due to water; (v) wavelengths above 940 nm are also affected by the falling efficiency of the silicon SPAD.

Figures 6(c) and (d), on the other hand, show the relative contributions obtained by fitting directly with the absorption spectra of commonly found biological chromophores, namely: deoxy-haemoglobin (HHb), water and lipids. Due to the speck being processed industrially and stored, oxy-haemoglobin was removed from the fitting process as it is not expected to be found after such long periods, as indeed was the case with the preliminary analysis. Further, collagen was also removed from the fitting as it has been shown to be predominant mainly at around 1060 nm [50]. As can be observed from both the figures, the concentration of HHb starts to increase with decreasing Z, from around 1 cm onward, and can be attributed to the blood components in the speck inclusion. Conversely, in the water background phantom in figure 6(c), as the probe moves closer to the inclusion, one notices a reduction in the contribution due to water and no contribution due to the lipids. This can be explained due to the inclusion having less water content, and little to none lipid contents. Similarly, in the lipid background matrix phantom, a decrease in the contribution due to lipids, and interestingly, a slight increase in the contribution due to water are noted as Z decreases, and arises due to the water content present in the speck.

However, using the absorption spectra of biological chromophores is not completely correct as the samples are heavily processed and stored, and cannot be considered close to an *in-vivo* situation for a component analysis. It would not be correct to say oxy or deoxy-haemoglobin, but rather just blood components. Thus, while the chromophore component analysis is a more real-life application-oriented approach, the inclusion versus background contribution is more apt in this scenario. Further, all the points elaborated previously for the non-physical values obtained in figures 6(b) such as noisy spectra, homogeneous model analysis, spectral resolution, etc, are also applicable here, and hence, these analyses provide predominantly qualitative results. Yet, the figures indeed corroborate the obtained spectral information with the experimental sample structure. Finally, in all the analyses, the background contribution does not drop to zero at $Z = 0$ due to the presence of background matrix contamination due to the homogeneous medium model used, as explained previously, however it still allows us to detect the presence of an inclusion spectrally, as envisaged before.

6. Conclusion

In conclusion, we demonstrated, for the first time the use of bioresorbable fibers for interstitial broadband spectroscopy using TD-DOS in the NSDS scenario. Bioresorbable fibers have been shown to have great scope in the medical field, and TD-DOS in NSDS configuration could be another option for the use of these CPG bioresorbable fibers in an interstitial setting. In particular, we envisage the possibility to use this approach for monitoring healing processes of surge of inflammation from within the treated organ. The capability of TD-DOS to disentangle absorption from scattering effects and the independence from amplitude fluctuations is a plus for reliable tracking of the assessed site.

By utilizing a fast-gated SPAD, we were able to perform interstitial, null-distance measurements using the bioresorbable fibers. We demonstrated good linearity in the absorption estimation up to $\mu_a = 0.35$ cm^{-1}. We were able to verify again our hypothesis of scattering-independent absorption retrieval, by obtaining the water absorption spectrum in the 700–940 nm range independent of the background scattering. Also, we were able to detect the presence of a speck inclusion in an aqueous as well as a lipid based background from about 1 cm of distance, identifying key spectral features of the inclusion.

Further improvements should aim to reduce the noise in the retrieved spectra and approach an *in-vivo* scenario. Possible directions are adoption of detectors with higher efficiencies in the near-infrared and the short-wave infrared regions to better resolve the water peak, single fiber spectroscopy with a specialized splicing, studies on signal acquisition as a function of fiber dissolution and breakage, to name a few.

Data availability statement

The data that support the findings of this study will be openly available following an embargo at the following URL/DOI: 10.5281/zenodo.8426219. Data will be available from 31 January 2025 [51].

(iii) European Union's NextGeneration EU Programme with the I-PHOQS Infrastructure—IR0000016, ID D2B8D520, CUP B53C22001750006

Conflict of interest

The authors declare no conflict of interest.

ORCID iDs

Vamshi Damagatla ⬤ https://orcid.org/0000-0003-4140-387X
Nadia G Boetti ⬤ https://orcid.org/0000-0002-5269-2390
Laura Di Sieno ⬤ https://orcid.org/0000-0002-3028-3705
Diego Pugliese ⬤ https://orcid.org/0000-0002-6431-1655
Ilaria Bargigia ⬤ https://orcid.org/0000-0003-4428-7958
Davide Janner ⬤ https://orcid.org/0000-0001-7954-979X
Alberto Dalla Mora ⬤ https://orcid.org/0000-0002-2783-6217
Antonio Pifferi ⬤ https://orcid.org/0000-0002-2261-2089

References

[1] Greatbatch W and Holmes C F 1991 *IEEE Eng. Med. Biol. Mag.* **10** 38–41
[2] Seitz J M, Durisin M, Goldman J and Drelich J W 2015 *Adv. Healthcare Mater.* **4** 1915–36
[3] Waris E, Konttinen Y T, Ashammakhi N, Suuronen R and Santavirta S 2004 *Expert Rev. Med. Devices* **1** 229–40
[4] Pina S and Ferreira J M F 2012 *J. Healthcare Eng.* **3** 243–60
[5] Prakasam M, Locs J, Salma-Ancane K, Loca D, Largeteau A and Berzina-Cimdina L 2017 *J. Funct. Biomater.* **8** 44
[6] Tao H *et al* 2012 *Proc. Natl Acad. Sci.* **109** 19584–9
[7] Huby N, Vié V, Renault A, Beaufils S, Lefevre T, Paquet-Mercier F, Pézolet M and Bêche B 2013 *Appl. Phys. Lett.* **102** 123702
[8] Dupuis A, Guo N, Gao Y, Godbout N, Lacroix S, Dubois C and Skorobogatiy M 2007 *Opt. Lett.* **32** 109–11
[9] Ceci-Ginistrelli E, Pugliese D, Boetti N G, Novajra G, Ambrosone A, Lousteau J, Vitale-Brovarone C, Abrate S and Milanese D 2016 *Opt. Mater. Express* **6** 2040–51
[10] Meena Narayana Menon D, Pugliese D, Giardino M and Janner D 2023 *Materials* **16** 3899
[11] Keereweer S, Van Driel P B, Snoeks T J, Kerrebijn J D, Baatenburg de Jong R J, Vahrmeijer A L, Sterenborg H J and Löwik C W 2013 *Clin. Cancer Res.* **19** 3745–54
[12] Grosenick D, Cantow K, Arakelyan K, Wabnitz H, Flemming B, Skalweit A, Ladwig M, Macdonald R, Niendorf T and Seeliger E 2015 *Biomed. Opt. Express* **6** 309–23
[13] Svensson T, Andersson-Engels S, Einarsdóttír M and Svanberg K 2007 *J. Biomed. Opt.* **12** 014022
[14] Dabrowski J M and Arnaut L G 2015 *Photochem. Photobiol. Sci.* **14** 1765–80
[15] Bossi A, Bianchi L, Saccomandi P and Pifferi A 2024 *Biomed. Opt. Express* **15** 2481–97
[16] Pandayil J T, Boetti N G and Janner D 2024 *J. Funct. Biomater.* **15** 79
[17] Alerstam E, Svensson T, Andersson-Engels S, Spinelli L, Contini D, Mora A D, Tosi A, Zappa F and Pifferi A 2012 *Opt. Lett.* **37** 2877–9
[18] Baran T M, Fenn M C and Foster T H 2013 *J. Biomed. Opt.* **18** 107007
[19] Svanberg K, Bendsoe N, Axelsson J, Andersson-Engels S and Svanberg S 2010 *J. Biomed. Opt.* **15** 041502
[20] Scholkmann F, Kleiser S, Metz A J, Zimmermann R, Pavia J M, Wolf U and Wolf M 2014 *NeuroImage* **85** 6–27
[21] Fantini S and Sassaroli A 2020 *Front. Neurosci.* **14** 519087
[22] Pifferi A, Contini D, Dalla Mora A, Farina A, Spinelli L and Torricelli A 2016 *J. Biomed. Opt.* **21** 091310
[23] Durduran T, Choe R, Baker W B and Yodh A G 2010 *Rep. Prog. Phys.* **73** 076701
[24] Torricelli A, Contini D, Dalla Mora A, Pifferi A, Re R, Zucchelli L, Caffini M, Farina A and Spinelli L 2014 *Funct. Neurol.* **29** 223
[25] Taroni P, Pifferi A, Torricelli A, Comelli D and Cubeddu R 2003 *Photochem. Photobiol. Sci.* **2** 124–9
[26] Konugolu Venkata Sekar S, Lanka P, Farina A, Dalla Mora A, Andersson-Engels S, Taroni P and Pifferi A 2019 *Appl. Sci.* **9** 5465
[27] Torricelli A, Pifferi A, Spinelli L, Cubeddu R, Martelli F, Bianco S D and Zaccanti G 2005 *Phys. Rev. Lett.* **95** 078101
[28] Del Bianco S, Martelli F and Zaccanti G 2002 *Phys. Med. Biol.* **47** 4131
[29] Martelli F, Binzoni T, Pifferi A, Spinelli L, Farina A and Torricelli A 2016 *Sci. Rep.* **6** 1–14
[30] Pifferi A, Torricelli A, Spinelli L, Cubeddu R, Martelli F, Zaccanti G, Del Bianco S, Tosi A, Zappa F and Cova S 2006 Time-resolved diffuse reflectance at null source-detector separation: a novel approach to photon migration *Biomedical Topical Meeting* (Optica Publishing Group) p TuD5
[31] Pifferi A *et al* 2008 *Phys. Rev. Lett.* **100** 138101
[32] Dalla Mora A, Di Sieno L, Re R, Pifferi A and Contini D 2020 *Appl. Sci.* **10** 1101
[33] Dalla Mora A *et al* 2015 *Biomed. Opt. Express* **6** 1749–60
[34] Mazurenka M, Di Sieno L, Boso G, Contini D, Pifferi A, Dalla Mora A, Tosi A, Wabnitz H and Macdonald R 2013 *Biomed. Opt. Express* **4** 2257
[35] Di Sieno L *et al* 2016 *Rev. Sci. Instrum.* **87** 035118
[36] Pifferi A *et al* 2005 *Appl. Opt.* **44** 2104–14
[37] Wabnitz H *et al* 2014 *J. Biomed. Opt.* **19** 086010
[38] Di Sieno L, Boetti N G, Dalla Mora A, Pugliese D, Farina A, Sekar S K V, Ceci-Ginistrelli E, Janner D, Pifferi A and Milanese D 2018 *J. Biophoton.* **11** e201600275
[39] Damagatla V, Boetti N G, Di Sieno L, Bargigia I, Negretti F, Pugliese D, Janner D, Spinelli L, Farina A and Pifferi A 2024 Use of bioresorbable fibers for short-wave infrared spectroscopy using time-domain diffuse optics *Biomed. Opt. Express* **15** 5041
[40] Sglavo V M, Pugliese D, Sartori F, Boetti N G, Ceci-Ginistrelli E, Franco G and Milanese D 2019 *J. Alloys Compd.* **778** 410–7

[41] Sekar S K V *et al* 2016 *IEEE J. Sel. Top. Quantum Electron.* **22** 406–14

[42] Bargigia I *et al* 2012 *Appl. Spectrosc.* **66** 944–50

[43] Dalla Mora A, Tosi A, Zappa F, Cova S, Contini D, Pifferi A, Spinelli L, Torricelli A and Cubeddu R 2009 *IEEE J. Sel. Top. Quantum Electron.* **16** 1023–30

[44] Martelli F 2009 *Light Propagation Through Biological Tissue and Other Diffusive Media: Theory, Solutions and Software* (SPIE Press)

[45] Bigio I J and Fantini S 2016 *Quantitative Biomedical Optics: Theory, Methods and Applications* (Cambridge University Press)

[46] Damagatla V, Lanka P, Brodu A, Noordzij N, Qin-Dregely J, Farina A and Pifferi A 2023 *J. Biomed. Opt.* **28** 121202

[47] Press W H, Teukolsky S A, Vetterling W T and Flannery B P 2007 *Numerical Recipes 3rd edn: The art of Scientific Computing* (Cambridge University Press)

[48] Spinelli L *et al* 2014 *Biomed. Opt. Express* **5** 2037–53

[49] Lanka P, Bianchi L, Farina A, De Landro M, Pifferi A and Saccomandi P 2022 *Sci. Rep.* **12** 14300

[50] Mule N, Maffeis G, Cubeddu R, Santangelo C, Bianchini G, Panizza P and Taroni P 2024 *Biomed. Opt. Express* **15** 4842–58

[51] Damagatla V *et al* 2025 *Bioresorbable fibers for interstitial null-separation diffuse optical spectroscopy using fast temporal gating Zenodo* https://doi.org/10.5281/zenodo.8426219